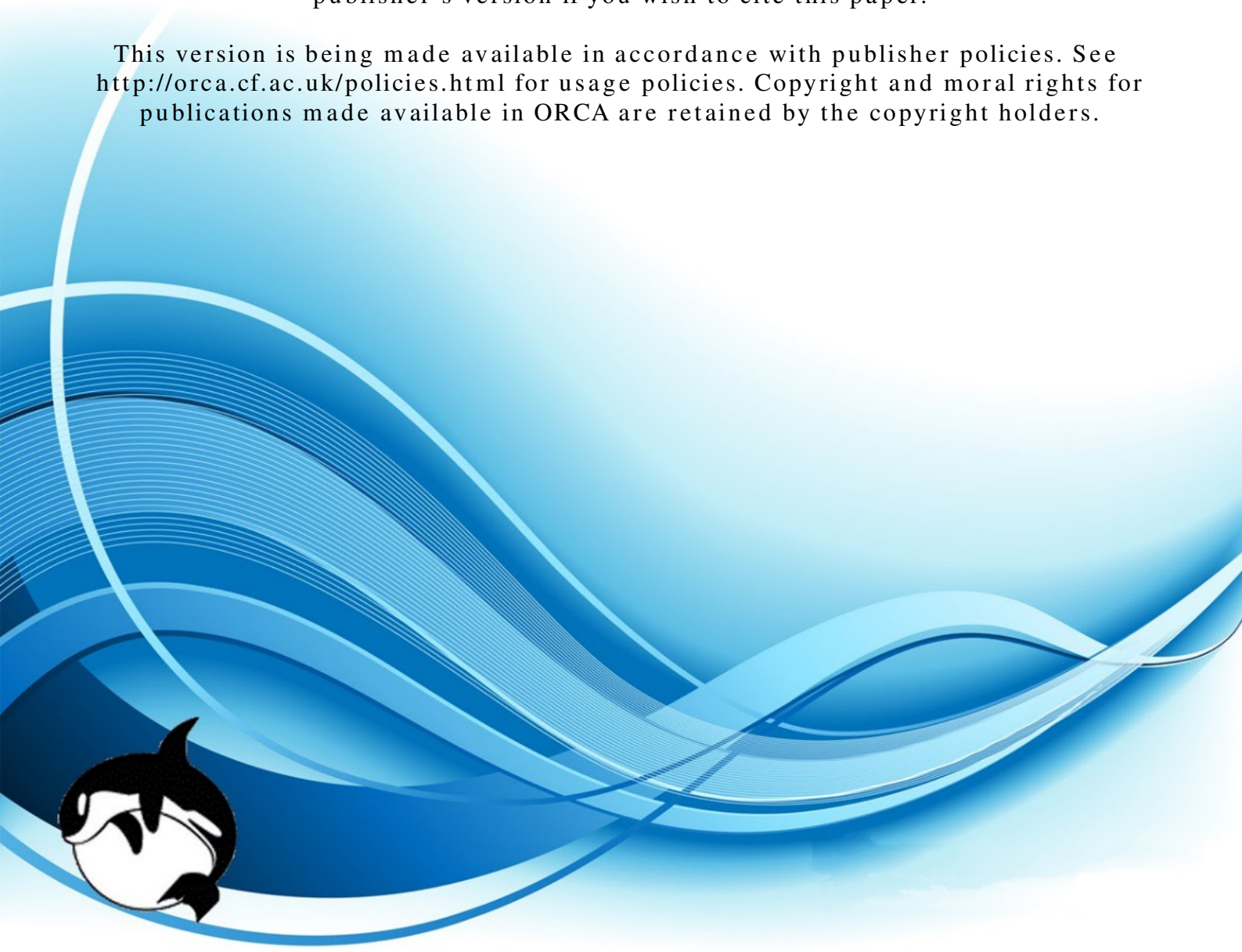

Electrical Impedance Tomography meets Reduced Order Modelling: a framework for faster and more reliable electrical conductivity estimations

Matthew R. Walker and Leandro Beltrachini. *†

Abstract

Inclusion of individualised electrical conductivities of head tissues is crucial for the accuracy of electrical source imaging techniques based on electro/magnetoencephalography. Parametric electrical impedance tomography (pEIT) is a method to cheaply and non-invasively estimate them using electrode arrays on the scalp to apply currents and measure the resulting potential distribution. Conductivities are then estimated by iteratively fitting a forward model to the measurements, incurring into prohibitively computational cost that is generally lowered at the expense of accuracy. Here, we introduce reduced order modelling (ROM) to massively speed up the calculations of these solutions for arbitrary conductivity values. We demonstrate this new ROM-pEIT framework using a realistic head model with 6 tissue compartments, with minimal errors in both the approximated numerical solutions and conductivity estimations. We show that the computational complexity required to reach a multi-parameter estimation with a negligible relative error is reduced by an order of magnitude when using this framework. Moreover, we demonstrate that the relative error in the estimations of all tissue compartments is at least half of that of previous methods with a typical reduction in error of an order of magnitude, even in the presence of noise. As a result, this framework can transform the use of pEIT for seeking personalised head conductivities, making it a valuable tool for researchers and clinicians.

1 Introduction

Characterising the electromagnetic activity in the brain is essential for understanding its function in health and disease. The preferred methods to measure this activity are electroencephalography (EEG) and magnetoencephalography (MEG), forming the foundation of electrical source imaging (ESI) techniques. ESI methods rely on computational models of head tissues including anatomical structure and physical properties such as the electrical conductivity field [1]. The use of realistic and individualised head models has been shown to greatly improve the accuracy of these methods [2, 3]. To generate these models, anatomical structure can generally be obtained from magnetic resonance or computerised tomography images using existing tools [4]. However, electrical conductivities are typically selected as a population average for each tissue. A recent analysis has shown that conductivity values in all human head tissues likely vary significantly between individuals, challenging

*This work is supported by the UKRI AIMLAC CDT, funded by grant EP/S023992/1.

†Both authors are with Cardiff University Brain Research Imaging Centre (CUBRIC), School of Physics and Astronomy, Cardiff University, UK.

these assumptions [5]. Moreover, studies have shown that inaccurate conductivity values lead to errors in source localisation in EEG/MEG [2, 6–9] and current localisation in transcranial electrical stimulation (TES) [10, 11]. Therefore, there exists a need to estimate these conductivities on an individual basis.

Parametric electrical impedance tomography (pEIT) is a relatively affordable and non-invasive method for estimating the conductivities of tissues in a human head [12]. Using an array of electrodes placed on the scalp, a small current is injected and extracted from a subset and the electrical potential is measured on the complementary set. This technique seeks to estimate the conductivities of head tissues by simulating forward solutions for sets of parameters and tuning the set to best match the electrical potential measurements taken. This allows one to characterise an individualised conductivity field. As this model becomes more detailed, the computational expense of these simulations increases, presenting a serious limitation for highly realistic models where pEIT can take days to complete on a standard PC.

The current best effort to address this issue is to reduce the number of solutions required for pEIT to converge by utilising a gradient assisted optimisation method [13]. This approach has proven successful for estimating scalp and skull conductivities from *in vivo* and synthetic measurements to a good level of accuracy [14, 15]. However, this method requires the additional calculation of a gradient in each iteration, which itself is computationally costly. Furthermore, estimating the conductivity of some tissues proves challenging. For example, the conductivity of the spongiform bone inside the skull has been estimated with a coefficient of variation as large as 1 [14].

In this work, we apply reduced order modelling (ROM) directly to pEIT to alleviate the computational demand while simultaneously improving conductivity estimations. ROM is a method utilised to find approximate numerical solutions to a parameterised boundary value problem quickly and accurately [16]. This process consists of a computationally intensive offline training phase and a real-time online phase. During the offline phase, a reduced order model is constructed using solutions to the boundary value problem at different points in a multi-dimensional parameter space. The online phase then utilises this model for real-time approximations of solutions for any set of parameters. We show that this framework yields significant improvements in the accuracy and speed of the estimation of all tissues in the head, assimilating the new capability to confidently estimate conductivities previously unreachable.

2 Methods

2.1 Parametric EIT Formulation

Parametric EIT is an ill-posed inverse problem (IP) that results in estimates of the electrical conductivities of tissue compartments. This is done by iteratively minimising the squared error between the measurements $\boldsymbol{y} \in \mathbb{R}^L$ and the conductivity-dependent simulated signals $\boldsymbol{U} \in \mathbb{R}^L$ on L electrodes. Mathematically, this is generally expressed as

$$\hat{\boldsymbol{\sigma}} = \arg\min_{\boldsymbol{\sigma}} \{(\boldsymbol{y} - \boldsymbol{U}(\boldsymbol{\sigma}))^T (\boldsymbol{y} - \boldsymbol{U}(\boldsymbol{\sigma}))\}, \tag{1}$$

where $\hat{\boldsymbol{\sigma}}$ are the estimated conductivities [15]. This results in an optimisation process that requires the calculation of one or more forward problems (FPs) at each iteration and then updating $\boldsymbol{\sigma}$ based on the error and the optimisation technique used (Fig. 1).

The pEIT-FP is a boundary value problem governed by a Laplace equation subject to Neumann boundary conditions [17]. The formulation and numerical methods for the pEIT-FP solution are well documented in the literature [14, 15, 17–19]. Here, we adopt the finite element (FE) method

due to its flexibility to handle arbitrary compartments. The variational formulation of the pEIT-FP considering the complete electrode model (CEM) [17, 20] results in the system [19]

$$\boldsymbol{A}(\boldsymbol{\sigma})\boldsymbol{u}(\boldsymbol{\sigma}) = \boldsymbol{b}, \tag{2}$$

where,

$$\boldsymbol{A}(\boldsymbol{\sigma}) = \begin{bmatrix} \boldsymbol{K}(\boldsymbol{\sigma}) & -\boldsymbol{B} \\ -\boldsymbol{B}^T & \boldsymbol{C} \end{bmatrix}, \tag{3a}$$

$$\boldsymbol{u}(\boldsymbol{\sigma}) = \begin{bmatrix} \boldsymbol{u}_n(\boldsymbol{\sigma}) \\ \boldsymbol{U}(\boldsymbol{\sigma}) \end{bmatrix}, \boldsymbol{b} = \begin{bmatrix} \boldsymbol{0} \\ \boldsymbol{I} \end{bmatrix}, \tag{3b}$$

$u_n(\boldsymbol{\sigma}) \in \mathbb{R}^n$ is the solution vector on the n nodes of the volumetric FE mesh and $\boldsymbol{I} \in \mathbb{R}^L$ is the vector of injection currents on the electrodes. The matrix $\boldsymbol{K}(\boldsymbol{\sigma}) \in \mathbb{R}^{n\times n}$ is known as the stiffness matrix and depends on the conductivity values of each compartment $\boldsymbol{\sigma} = \{\sigma_1, \sigma_2, ..., \sigma_P\}$, where P is the number of tissue compartments. The matrices $\boldsymbol{B} \in \mathbb{R}^{n\times L}$ and $\boldsymbol{C} \in \mathbb{R}^{L\times L}$ encode information about the electrodes on the surface of the domain and do not depend on the conductivity. The entries of the matrices $\boldsymbol{K}$, $\boldsymbol{B}$ and the diagonal matrix $\boldsymbol{C}$ are given by [21]

$$K_{ij} = \int_\Omega \langle \sigma \nabla\psi_i, \nabla\psi_j \rangle d\Omega + \sum_{l=1}^{L} \frac{1}{z_l} \int_{e_l} \psi_i \psi_j d(\partial\Omega), \tag{4a}$$

$$B_{il} = \frac{1}{z_l} \int_{e_l} \psi_i d(\partial\Omega), \tag{4b}$$

$$C_{ll} = \frac{1}{z_l} \int_{e_l} d(\partial\Omega) = \frac{|e_l|}{z_l}, \tag{4c}$$

where e_l represents the lth electrode, $|e_l|$ its area, z_l its contact impedance, Ω is the domain (i.e., the head) with boundary $\partial\Omega$, and ψ_i is a basis function on the nodes $i = 1, 2, ..., n$.

A useful property of the matrix $\boldsymbol{K}(\boldsymbol{\sigma})$ is that, in the case of homogeneous conductivities, it can be linearly decomposed into several constituent stiffness matrices $\boldsymbol{K}_p \in \mathbb{R}^{n\times n}$, each representing a different compartment p in the head model and independent of $\boldsymbol{\sigma}$. Consequently, the matrix $\boldsymbol{A}(\boldsymbol{\sigma})$ can be split into p matrices $\boldsymbol{A}_p \in \mathbb{R}^{(n+L)\times(n+L)}$,i.e.,

$$\boldsymbol{A}(\boldsymbol{\sigma}) = \boldsymbol{A}_0 + \sum_{p=1}^{P} \sigma_p \boldsymbol{A}_p, \tag{5}$$

where $\boldsymbol{A}_0$ is a $\boldsymbol{\sigma}$-independent matrix encoding the information from matrices $\boldsymbol{B}$ and $\boldsymbol{C}$ and the second term in eq. (4a). It is straightforward to show that such a decomposition holds even in the case of anisotropic conductivities [15]. This property is referred to as *affine decomposition* of the parameters of interest (i.e., the conductivities) and it is a fundamental requirement for a system where ROM is applied.

2.2 Reduced Order Modelling

ROM is a mathematically rigorous technique to efficiently build a low-dimensional model mapping changes in a set of conductivities to changes in the solution of eq. (2) [16]. This model is constructed in an offline phase using a relatively small number of $N << (n+L)$ strategically selected solutions of eq. (2) with specific conductivities, which are then used in the 'online' phase to find rapid solutions

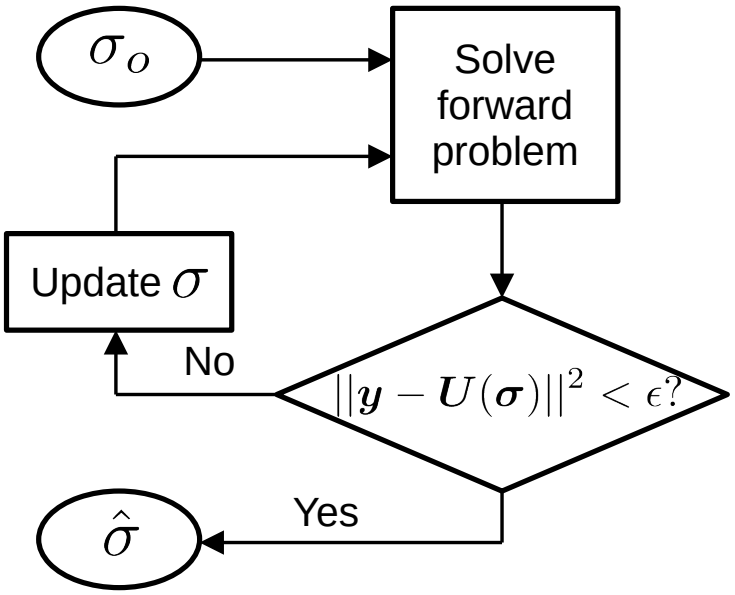

Fig. 1: Flow chart of the traditional implementation of the inverse problem for pEIT. Here, ϵ refers to a stopping threshold, $\boldsymbol{\sigma_0}$ is the initial conductivity guess and $\hat{\boldsymbol{\sigma}}$ is the estimated conductivity value. Note that each loop requires at least a full calculation of the forward problem.

for any set of conductivities. Below, we present a brief overview of the fundamental principles of ROM.

Taking advantage of the affine decomposition, massively reduced versions of the $\boldsymbol{A}_p$ matrices can be formed using the reduced model, allowing the assembly of a reduced system in the online phase at any point in the P-dimensional parameter space $\mathscr{P} \in \mathbb{R}^P$ (i.e., for any set of conductivities). This new system can be solved in real-time, resulting in a reduced-basis solution $\boldsymbol{u}_N \in \mathbb{R}^N$ that is transformed to $\boldsymbol{u}_a \in \mathbb{R}^{n+L}$ approximating the solution of the high-dimensional system $\boldsymbol{u}$.

The model is trained using a number of full-order solutions, called snapshots, which are selected strategically across $\mathscr{P}$. Judiciously choosing the points with which to build the reduced model is done by employing a greedy algorithm. A distinguishing feature of ROM is the presence of a rigorous upper bound $\Delta(\boldsymbol{\sigma})$ on the error of the approximate solutions, which guides the greedy algorithm in the snapshot selection, acting as a proxy for the error [16]. This bound on the error can be calculated almost instantly for any given point in $\mathscr{P}$ and can therefore efficiently explore the space to guide the next snapshot point. During each iteration of the greedy algorithm, the bound is calculated for a finite sample set $\Xi \subset \mathscr{P}$ and a snapshot is calculated using the conductivity set that minimises it. Ξ is chosen to represent the entire P-dimensional space $\mathscr{P}$. Utilising the bound to select the snapshots presents two advantages. Firstly, it allows an extremely quick assessment of the maximum error attainable at a fine discritisation of $\mathscr{P}$. Secondly, it can be used as a stopping criterion for certifying the maximum error in $\boldsymbol{u}_a$ [16]. The relationship between the *a posteriori* relative error [$\mathrm{RE}(\boldsymbol{\sigma})$] for a given point in $\mathscr{P}$ and the *a posteriori* relative error bound [$\Delta_{RE}(\boldsymbol{\sigma})$] is [16]

$$\mathrm{RE}(\boldsymbol{\sigma}) \triangleq \frac{||\boldsymbol{u}(\boldsymbol{\sigma}) - \boldsymbol{u}_a(\boldsymbol{\sigma})||_{L_2}}{||\boldsymbol{u}_a(\boldsymbol{\sigma})||_{L_2}} \leq \frac{\Delta(\boldsymbol{\sigma})}{||\boldsymbol{u}_N(\boldsymbol{\sigma})||_{L_2}} \triangleq \Delta_{RE}(\boldsymbol{\sigma}). \tag{6}$$

The reduced model takes the form of a reduced-basis space, built using the snapshots calcu-

lated by the greedy algorithm. To obtain the reduced system, the full-order stiffness matrices are projected on the space during the offline phase. This reduced-basis space is represented by the matrix $\mathbb{V} \in \mathbb{R}^{(n+L)\times N}$. To construct the orthonormal basis, $\mathbb{V}$ we perform a Gram-Schmidt orthonormalisation on a snapshot, before adding it to the orthonormal basis iteratively. We begin by selecting a random parameter vector $\boldsymbol{\sigma}_1 \in \Xi$ and computing the full-order solution $\boldsymbol{u}(\boldsymbol{\sigma}_1)$. The first basis vector for the orthonormal space is simply the first snapshot, which is a full-order solution (i.e., $\boldsymbol{\zeta}_1(\boldsymbol{\sigma}_1) = \boldsymbol{u}(\boldsymbol{\sigma}_1)$). Thereafter, the orthonormalised solutions $\boldsymbol{\zeta}_j(\boldsymbol{\sigma})$ for the jth snapshot are concatenated,

$$\mathbb{V} = [\boldsymbol{u}(\boldsymbol{\sigma}_1), \boldsymbol{\zeta}_2(\boldsymbol{\sigma}_2), ..., \boldsymbol{\zeta}_N(\boldsymbol{\sigma}_N)], \tag{7}$$

such that $\{\boldsymbol{\sigma}_1, \boldsymbol{\sigma}_2, ..., \boldsymbol{\sigma}_N\} \subset \Xi$. Also known as the transformation matrix, $\mathbb{V}$ relates the projected stiffness matrix $\boldsymbol{A}_N(\boldsymbol{\sigma}) \in \mathbb{R}^{N\times N}$ and projected independent vector $\boldsymbol{b}_N(\boldsymbol{\sigma}) \in \mathbb{R}^N$ with the full-order versions through the expressions [16]

$$\boldsymbol{A}_N(\boldsymbol{\sigma}) = \mathbb{V}^T \boldsymbol{A}(\boldsymbol{\sigma})\mathbb{V}, \;\; \boldsymbol{b}_N(\boldsymbol{\sigma}) = \mathbb{V}^T \boldsymbol{b}(\boldsymbol{\sigma}), \tag{8}$$

resulting in the reduced system to solve

$$\boldsymbol{A}_N(\boldsymbol{\sigma})\boldsymbol{u}_N(\boldsymbol{\sigma}) = \mathbf{b}_N(\boldsymbol{\sigma}), \tag{9}$$

where $\boldsymbol{u}_a(\boldsymbol{\sigma}) = \mathbb{V}\boldsymbol{u}_N(\boldsymbol{\sigma})$. It is clear from eq. (8) that, as $N << (n + L)$, the dimensions of the resulting system are massively reduced, requiring significantly fewer operations to solve. Ultimately, this means that a FP can be calculated at any point in $\mathscr{P}$ almost instantly. Fig. 2 shows a flowchart of the greedy algorithm, demonstrating the construction of $\mathbb{V}$.

Finally, it should be noted that the calculation of the bound relies on a $\boldsymbol{\sigma}$-dependent parameter called the stability factor $\beta_h(\boldsymbol{\sigma})$, related in the following way

$$\Delta(\boldsymbol{\sigma}) = \frac{||\boldsymbol{b} - \boldsymbol{A}(\boldsymbol{\sigma})\mathbb{V}\boldsymbol{u}_N(\boldsymbol{\sigma})||_{L_2}}{\beta_h(\boldsymbol{\sigma})} \; . \tag{10}$$

The numerator of eq. (10) is known as the residual and can be found very quickly with some computational splitting inside the greedy algorithm. Obtaining the stability factor, however, is a more computationally intensive calculation requiring the solution to a generalized eigenvalue problem [16]. Therefore, we employ a similar schema as before, splitting it into an offline training phase and online real-time phase. The offline phase involves creating an interpolant using radial basis functions and interpolation points in $\mathscr{P}$ which can then be used in the online phase for a quick evaluation of $\beta_h(\boldsymbol{\sigma})$ for any point in $\mathscr{P}$. For details on the splitting of the residual, calculation of the bound, its offline/online decomposition, and its calculation for a rank-deficient stiffness matrix, the reader is referred to Quarteroni et al. (2016) [16, Ch.3,4,6].

2.3 Implementation and Experiments

2.3.1 Set-up

We used a realistic head model discritised with 4M tetrahedral elements and 800k nodes. The model was based on the Colin27 atlas [22] and processed as in previous publications [2]. A cross section is shown in Fig. 3a depicting different tissue compartments, i.e., scalp, compact skull bone, spongiform bone, cerebrospinal fluid (CSF), grey matter (GM) and white matter (WM). The conductivities chosen for the synthetic measurements were uniform random samples within the ranges described in Table 1 for each of the tissues. These ranges were chosen to be consistent with the work carried out by McCann et al. (2019) [5]. A reduced model for each electrode pair used was trained for conductivity parameters within these ranges.

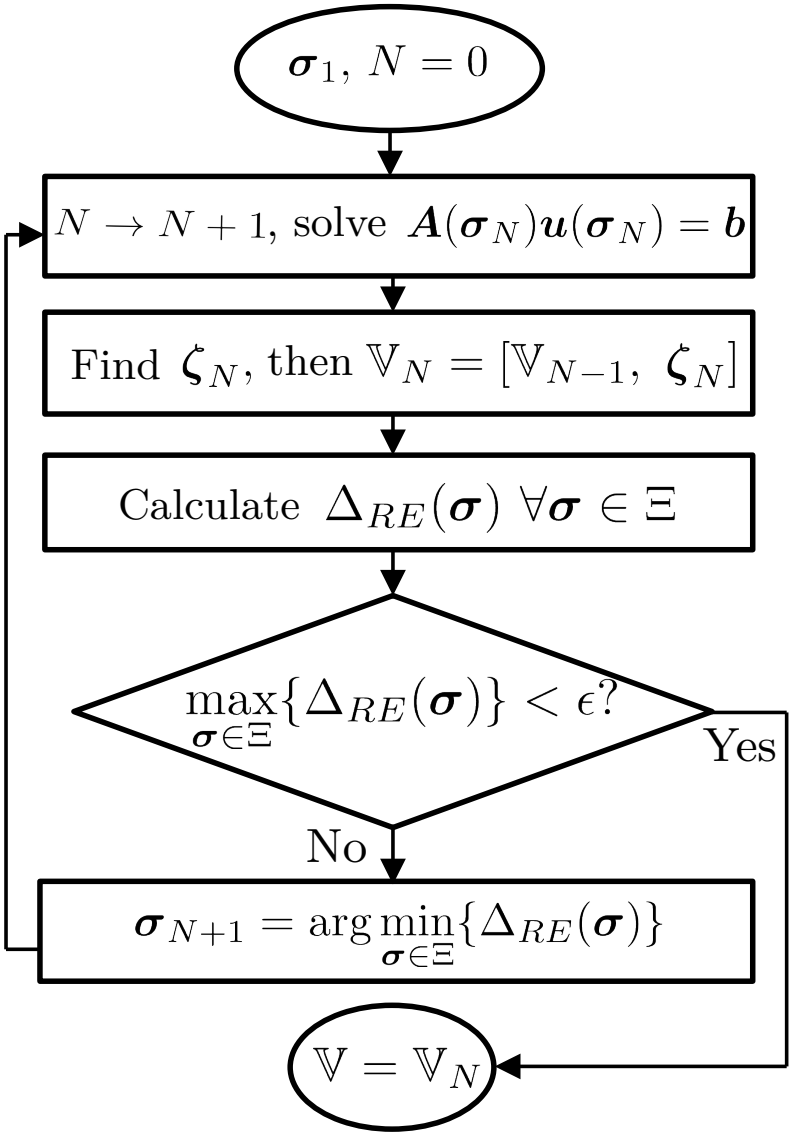

Fig. 2: Greedy algorithm used in the offline training phase for ROM where ϵ is some stopping threshold.

2.3.2 Technical Implementation

For each conductivity sample, the FP was solved for each of the 132 pairs of electrodes, where the injection and extraction electrode had 20 μA and -20 μA applied, respectively. All pairs are composed of a unique injection electrode and a sink electrode that is common for all pairs placed on the scalp above the Sagittal suture. The systems of equations were solved with the Preconditioned Conjugate Gradient (PCG) solver with incomplete LU preconditioners [23]. They were solved with

a tolerance of 10^{-10} and a maximum number of iterations of 6000. The Gaussian noise added to the measurements had a standard deviation of 0.82 μV, which is similar to the noise found in real measurements [14]. The 133 electrodes were modelled as 1 cm diameter circles on the surface of the scalp with an effective contact impedance of 5 Ωm^2.

The FE method was implemented using first-order linear basis functions on the mesh nodes as used by Vauhkonen et al. (1999) [19]. Analytical expressions of the element matrices needed in eqs. (4a)-(4c) were utilised to avoid errors due to numerical quadrature [24].

The ROM method was trained using the same model, injection patterns and range of conductivities as above. We chose to train ROM for up to 100 snapshots to demonstrate the reduction in error in the FPs and IPs. However, as will become clear, there are a number of stopping criteria that can guide how many snapshots to take.

Similarly to other work [14], we have removed some erroneous estimations from injection patterns where the IP has either not converged or has given an unrealistic conductivity (e.g., negative conductivities), which may occur for the traditional method only as it is based on an unconstrained optimisation technique.

2.3.3 Experiment 1 - ROM Performance

Our first experiment serves two main purposes. The first is to confirm that the pEIT-FP is meaningfully reducible in the sense that, for small N values, $\boldsymbol{u}_a$ quickly converges to $\boldsymbol{u}$. The second is to validate our bound while simultaneously assessing its tightness. To achieve these aims, we plotted the average and maximum RE($\boldsymbol{\sigma}$) and $\Delta_{RE}(\boldsymbol{\sigma})$ as a function of N. The $\Delta_{RE}(\boldsymbol{\sigma})$ was calculated in the training phase during the greedy algorithm for a 6000 sample train across $\mathscr{P}$ for each electrode pair. The mean and maximum $\Delta_{RE}(\boldsymbol{\sigma})$ across the sample train were found for each electrode pair and then averaged across all electrode pairs. The RE($\boldsymbol{\sigma}$) was calculated for each electrode pair for 100 samples of $\mathscr{P}$. The average RE($\boldsymbol{\sigma}$) across all electrodes for each sample was found before plotting the average and maximum across $\mathscr{P}$. This was repeated for an increasing number of snapshots.

2.3.4 Experiment 2 - IP Performance

To assess how useful the ROM-pEIT framework is, we considered two important metrics in pEIT: the accuracy of the estimations from the inverse problem and the computational cost required to achieve them. To that end, we compared our results with the best approach currently in the field, which provides reliable estimations for scalp and compact skull electrical conductivities [14]. This method minimises eq. (1) using the gradient-assisted quasi-Newton method. However, this requires the calculation of the gradient of the solution for each FP, for each of the parameters being searched for [14, 25]. The gradient can be found using [14]

$$\frac{\partial \mathbf{A}^{-1}(\boldsymbol{\sigma})\mathbf{b}}{\partial \sigma_p} = -\mathbf{A}^{-1}(\boldsymbol{\sigma})\mathbf{A}_p\boldsymbol{u}. \tag{11}$$

	Scalp	Compact bone	Spongiform bone	CSF	GM	WM
Min (S/m)	0.303	0.002	0.013	1.450	0.268	0.092
Max (S/m)	0.444	0.009	0.043	1.794	0.508	0.177

Tab. 1: Range of conductivities used for training.

From eq. (11), it is clear that finding each of the gradients requires solving another large system of equations similar to the FP. This results in a significant overhead in terms of computational cost, especially when multiple parameters are being estimated simultaneously. Inserting this into the loop in Fig. 1 shows that, for each iteration in the optimisation, the number of large systems of equations to solve is equal to the FP plus the number of tissues being estimated. Henceforth, we shall refer to this method of gradient assisted optimisation using the full-order FP as the traditional method.

A further consequence of using the reduced system of eqs. (9) is that the derivative (11) can no longer be calculated and therefore neither can the quasi-Newton method be utilised efficiently. However, using quasi-Newton methods to reduce the computational cost is no longer of concern, and we are free to explore other methods, such as the interior-point optimisation approach. Although this method requires more loops and therefore more systems to solve than the quasi-Newton algorithm, the cost of the new optimisation is still negligible compared to the traditional technique.

Therefore, we have chosen to compare the computational cost of the ROM-pEIT framework and the traditional method by using the number of $(n+L)\times(n+L)$ linear systems of equations needed to be solved for each electrode pair. For ROM, all of these systems are solved in the offline phase. Given that these systems embody the bulk of the computational work, it is an appropriate metric for comparison. Making the comparison independent of the electrode pairs means that the savings are the same irrespective of the injection protocols used.

For the traditional method, the IP was run as a 3-parameter search, optimising for the scalp, compact skull and spongiform bone simultaneously. For the conductivities not being optimised (CSF, GM, WM), they were fixed to the ground truth values used to make the synthetic measurements. We chose this format to isolate and assess the estimation of the three conductivities stated only. The estimation progress was logged at each iteration and plotted as the RE($\boldsymbol{\sigma}$) between the estimation and the sample parameters. The ROM IP was run as a 6-parameter search to estimate all of the compartments in the model. All optimisations were started from the centre point of the ranges specified in Table 1.

The mean of the relative error (RE) in the estimation for each tissue for each number of iterations (and function evaluations within those iterations) was calculated, and then averaged across 10 randomly selected conductivity samples. We used 10 samples due to the computational cost of the traditional method. The IP with ROM was then run for a further 90 samples of $\mathscr{P}$ and plotted separately with the average RE across the samples and electrodes displayed for all tissues.

2.3.5 Experiment 3 - Anisotropy

It has been shown that the inclusion of the spongiform bone in head models reduces the error in the EEG-FP and IP [2]. However, in the event of missing spongiform information, the skull may be modelled as a single compartment with anisotropic conductivity [15, 26]. Therefore, a separate experiment aimed to demonstrate the adaptation of ROM-pEIT to model a homogeneous and anisotropic skull conductivity.

Firstly, we modified the realistic head model by merging the compact and spongiform bone to create one homogeneous skull compartment. We then trained another ROM model with the new head model where the conductivity tensor field for the skull compartment has been transformed from a Cartesian basis to a radial and tangential basis relative to the centre point of the brain. The range of values used for both radial and tangential conductivities were from the minimum compact skull (0.002 S/m) to the maximum spongiform skull (0.043 S/m) used in the previous experiments. This was to accommodate for a wide range of possible skull compositions, from entirely compact skull to significant proportions of spongiform bone.

We analysed the sensitivity of the ROM-pEIT framework to anisotropic conductivities in the

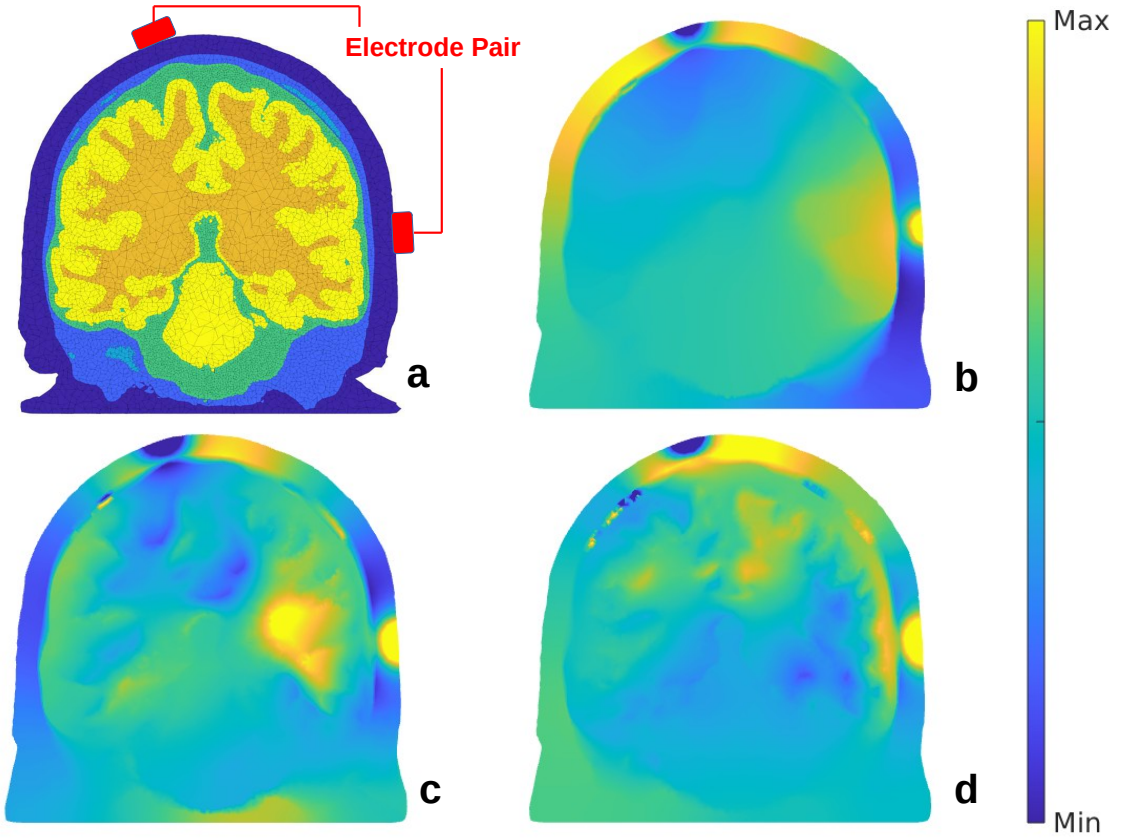

Fig. 3: **a**) Cross section of the FE mesh with compartments coloured separately. **b-d)** Selection of the first basis vectors ($\boldsymbol{\zeta}_2$, $\boldsymbol{\zeta}_4$ and $\boldsymbol{\zeta}_{11}$, respectively) for the transformation matrix $\mathbb{V}$ made for an electrode pair plotted on the FE mesh. The colour indicates the value of the projected basis vector at each node that represents the additional information being encoded.

skull by assessing the RE in each compartment. To achieve this, we created 100 synthetic measurements using the full-order model with noise. The model was adapted by merging the compact and spongiform skull and given an anisotropic conductivity in the same range used for ROM. These measurements were then used to run the IP with a new reduced model, trained with radial and tangential conductivities in the whole skull. We plotted the RE in the estimation for each tissue compartment to assess the sensitivity of the reduced basis IP to the radial and tangential components of the skull conductivity. As before, the IP was run as a 6-parameter estimation, this time estimating the radial and tangential values, replacing the compact and spongiform skull conductivities.

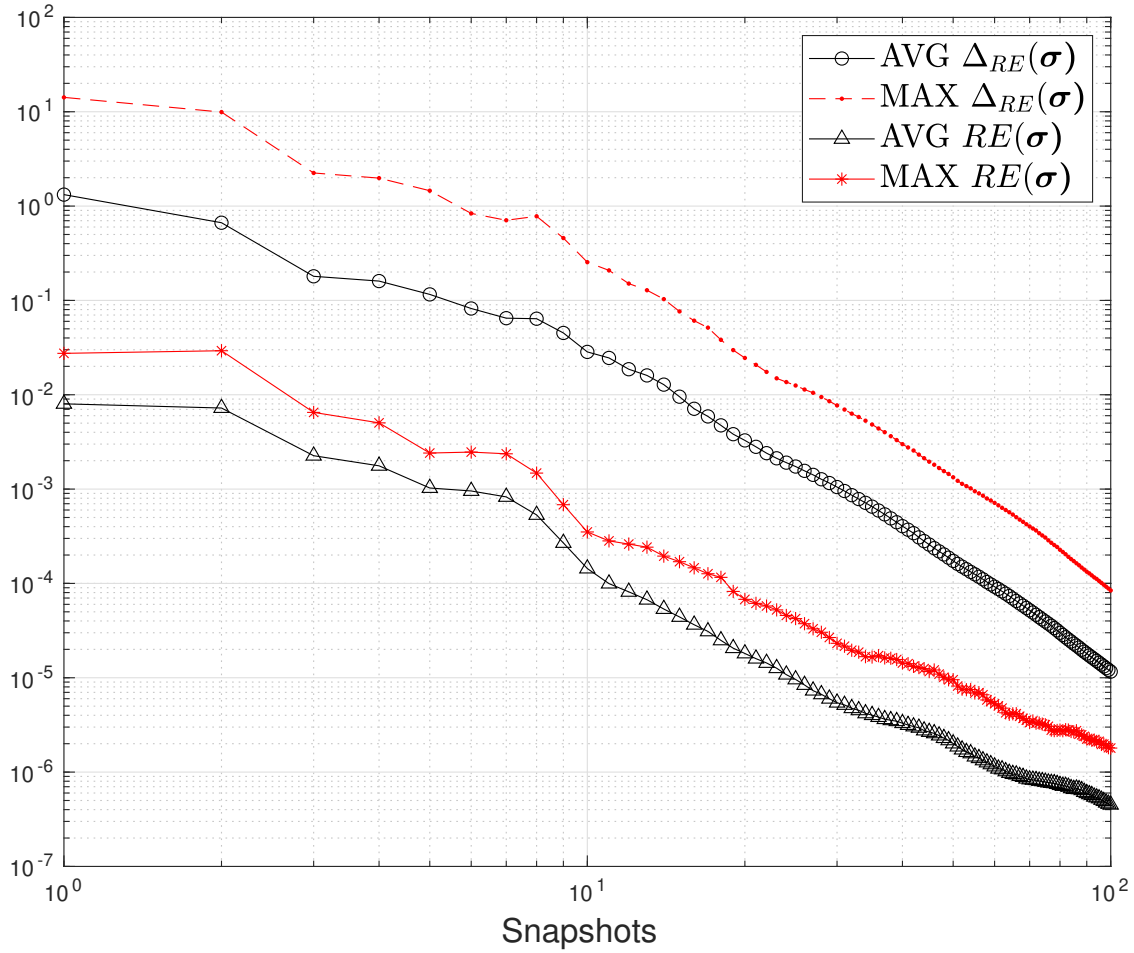

Fig. 4: Average and maximum $\Delta_{RE}(\boldsymbol{\sigma})$ and RE($\boldsymbol{\sigma}$) for a sample of parameters (averaged across electrodes) against the number of snapshots.

3 Results

3.1 Experiments

3.1.1 Experiment 1 - ROM Performance

Figs. 3b-d show a subset of the basis vectors (i.e., $\boldsymbol{\zeta}_i$ for $i = 2, 4, 11$) that constitute the reduced basis space. Each additional function to the first is an orthogonal projection to the matrix $\mathbb{V}$ and encodes additional information into the reduced model. In particular, the basis vector $\boldsymbol{\zeta}_{11}$ (Fig. 3d) shows that after the projection there is a significant difference in electrical potential solution in the brain between the previous sample conductivities and those for the snapshot. Once added, this results in a reduced model with specific information about the response of the electrical potential in the brain to conductivity changes in the model. This demonstrates the greedy algorithm in action. The same

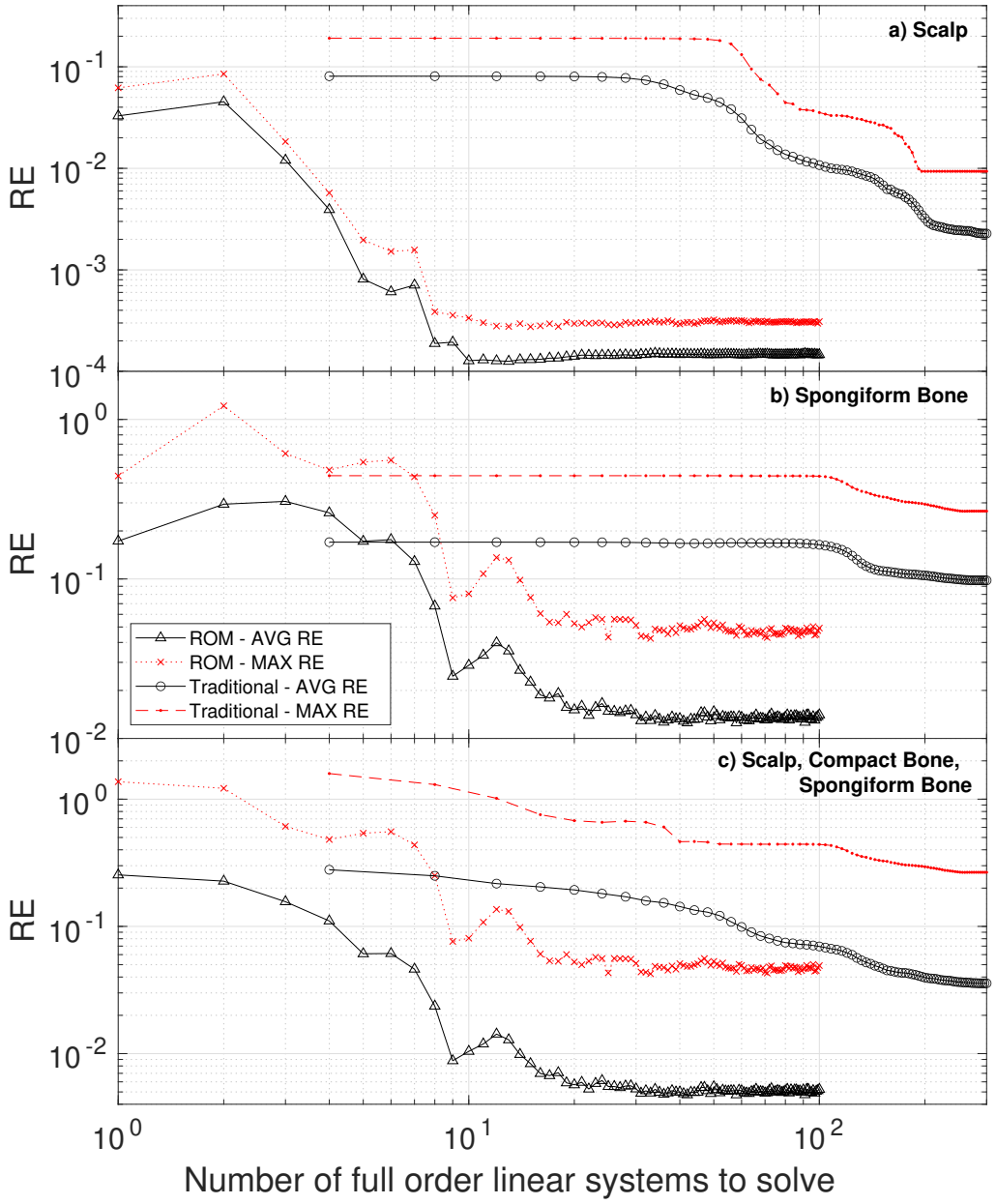

Fig. 5: Average (black lines) and maximum (red lines) of the RE in the estimation of the conductivities across multiple electrode pairs and for 10 sets of synthetic measurements with uniformly distributed conductivity samples. The red and black dotted lines in each figure correspond to the traditional method and the red and black full lines with crosses and triangles respectively are for ROM.

effect can be seen with the spongiform bone with respect to the bright spots in the skull in basis vector $\boldsymbol{\zeta}_4$ (Fig. 3c) and $\boldsymbol{\zeta}_{11}$.

Fig. 4 shows the average and maximum $\Delta_{RE}(\boldsymbol{\sigma})$ and RE($\boldsymbol{\sigma}$) as a function of snapshots. The $\Delta_{RE}(\boldsymbol{\sigma})$ was calculated across the sample set Ξ and the RE($\boldsymbol{\sigma}$) was found for 100 conductivity samples. It is interesting to note that the bound becomes slightly sharper as the number of snapshots increases. Fig. 4 also demonstrates that $\Delta_{RE}(\boldsymbol{\sigma})$ can be used as a stopping criteria for the number of snapshots used to train the model. When set, the greedy algorithm will stop when $\Delta_{RE}(\boldsymbol{\sigma})$ for every point in the fine sample is below the threshold stated. Using this stopping criteria ensures that the RE($\boldsymbol{\sigma}$) in the FP is below the threshold. However, choosing a threshold is not trivial (see Section 4) and there is a risk of unnecessary training of the model.

3.1.2 Experiment 2 - IP Performance

Displayed in Fig. 5 is the average and maximum RE in the conductivity estimations for ROM and the traditional method across 10 samples and all electrode pairs. It can be seen that there are improvements in computational cost and accuracy of the ROM-pEIT framework compared to the traditional method. This is shown for the first three compartments of the head model (scalp, compact skull and spongiform bone) and the scalp and spongiform bone separately. Focusing on the three compartment graph (Fig. 5c), we can see that the RE in the IP estimation averaged across compartments, injection patterns, samples of parameter space improves by nearly an order of magnitude, with the number of linear systems to solve reducing by an order of magnitude too. The maximum error for any injection pair for any sample is displayed in red crosses and also demonstrates an improvement over the average of the traditional method.

The number of injection pairs removed from the traditional estimations due to erroneous results was approximately 30 for two of the samples and none for the rest. All injection pairs were preserved for the ROM-pEIT IPs.

It is useful to separate all of the conductivities to see which are contributing the most to the REs seen in Fig. 5c. The RE for the scalp is shown in Fig. 5a, where the improvement in accuracy and computational effort due to the ROM-pEIT framework is most apparent with a reduction in systems to solve from 250 to 10 maintaining an order of magnitude improvement in RE. In Fig. 5b, we see that the traditional method cannot obtain a reliable estimate for the spongiform bone with the optimisation implementation used. However, the ROM-pEIT framework is able to estimate the conductivity of the spongiform bone down to an average RE of almost 1% and a maximum RE of 5%.

As previously mentioned, the benefits of using ROM become most clear during a 6-parameter search where the IP can optimise for all compartments in the model. Fig. 6 shows the average RE for ROM but for all tissue compartments, as a function of the number of snapshots used in the estimation. The figure shows us that with ROM and the optimisations it allows, the IP is able to estimate CSF, GM and WM in the brain to approximately a 3%, 4%, 7% RE, respectively. It is also worth noting that the coefficient of variation in the electrode estimations was between 0.001 and 0.1 for all tissues after 30 snapshots.

From Figs. 5 and 6 it is clear that the accuracy of the IP with ROM stops improving after 30 snapshots. Therefore, we chose to only train the anisotropic reduced model in Experiment 3 up to this number to perform the sensitivity analysis.

3.1.3 Experiment 3 - Anisotropy

The results of the sensitivity analysis described in Section 2.3.5 are displayed in Fig. 7. From this analysis we can see that the framework presented is sensitive to the tangential and radial conductivity

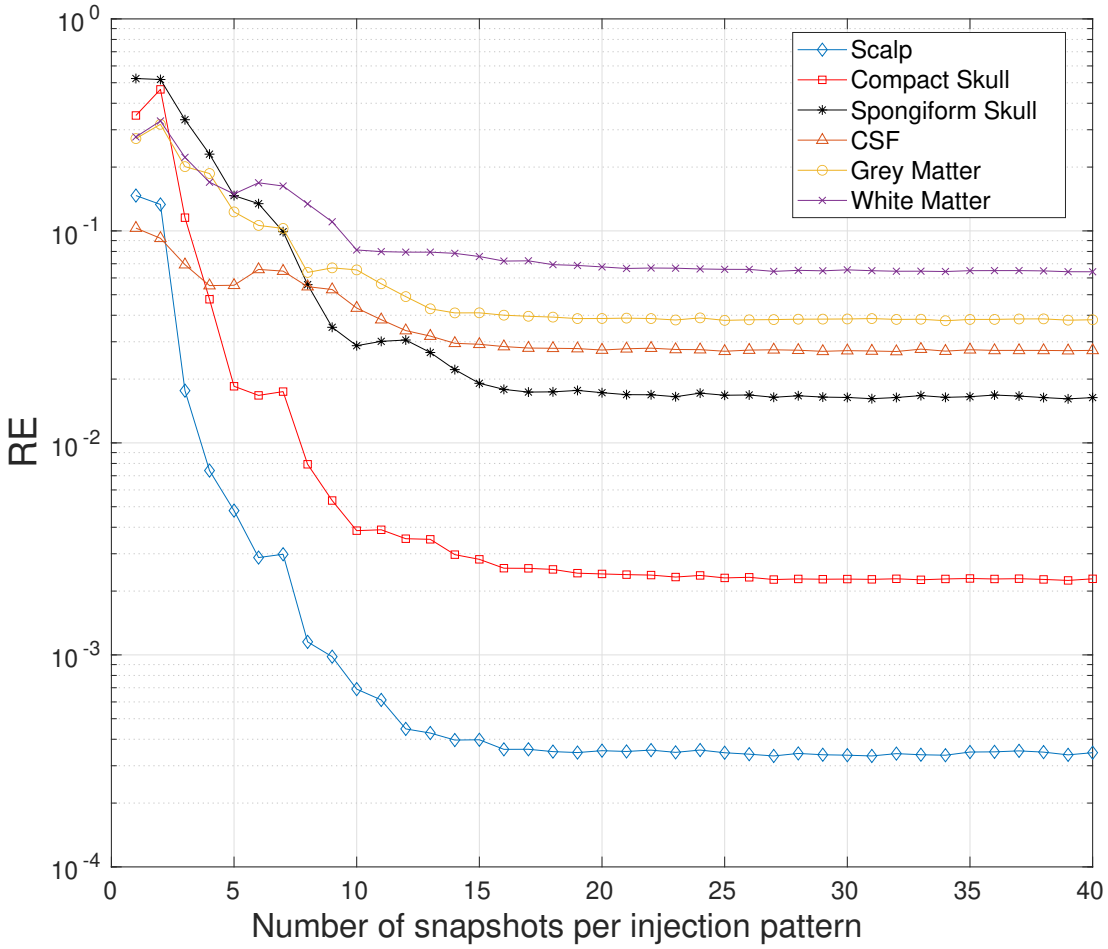

Fig. 6: RE for each individual compartment as a function of snapshots across 100 samples and 132 injection pairs using the ROM-pEIT method.

components of the skull while remaining sensitive to the inner compartments.

4 Discussion

We have presented a framework for the solution of the pEIT-FP using ROM, where we have demonstrated significant reductions in computational expense as compared to the current state-of-the-art approach. Similarly, we have shown that huge improvements can be achieved in conductivity estimations for all tissues, many previously unreachable by pEIT.

We have validated this approach experimentally by testing both methods on a realistic 6-layered head model to emulate typical use cases. Fig. 5 exhibits the speed up and accuracy improvement of using ROM-pEIT over the traditional method when the inner tissue conductivities are assumed to be known. A more realistic scenario would be that the inner tissue conductivities are unknown. In this instance, we found that after 200 full order systems solved the error in scalp estimations was half an

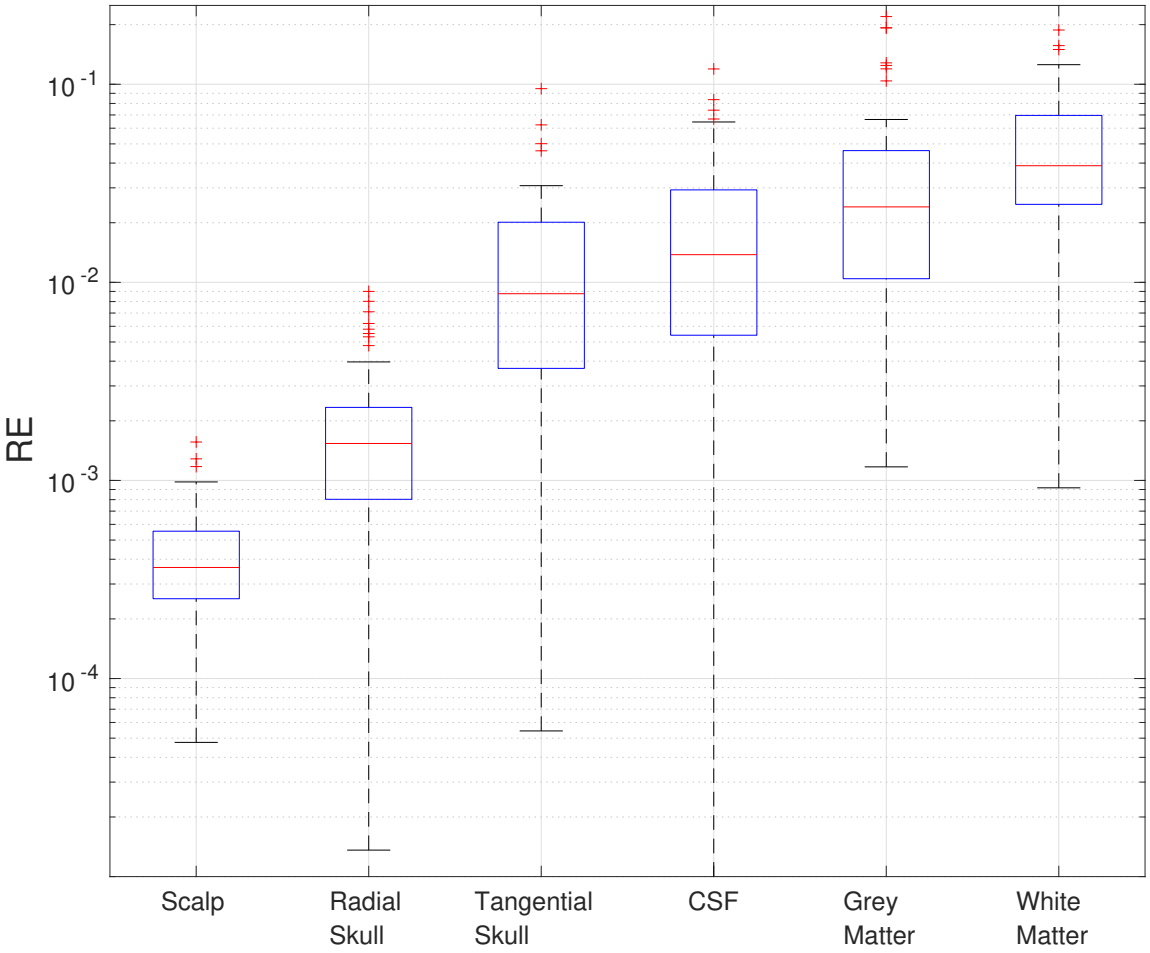

Fig. 7: Sensitivity Analysis across 100 samples for the reduced basis anisotropic model. The estimations are for the full 6-parameter space using 30 snapshots for each electrode pair. Each box plot shows the estimation error in a single tissue that is labelled.

order of magnitude higher than that achieved assuming the inner conductivities known (Fig. 5). We also found that the spongiform bone could not be estimated reasonably for the traditional algorithm.

For models that have been built from only T1-weighted MRI images, where segmenting spongiform bone in the skull accurately is not feasible, it has been shown to reduce errors in the EEG FP and IP when the anisotropy of the skull conductivity is considered [9]. In this context, ROM-pEIT also extends to such a situation. Fig. 7 also shows us that this IP is more sensitive to the radial conductivity than the tangential conductivity, which is consistent with reported findings [15]. The reduced anisotropic model is also bounded and we found that, for 30 snapshots, the mean $\Delta_{RE}(\boldsymbol{\sigma})$ was approximately 10^{-2} and the mean $\mathrm{RE}(\boldsymbol{\sigma})$ was 10^{-4}.

Some efforts have been made to avoid the computational expense of EIT while retrieving subject-specific conductivity values. Akalin Acar et al. (2016) [27] and Costa et al. (2017) [28] demonstrated techniques for the simultaneous estimation of the conductivity of the skull and the location of the

source of electrical activity. Others have used a pre-calibration technique for combined EEG and MEG where an initial conductivity value for the skull is given and then tuned before the source localisation by using somatosensory evoked potential data [29–31]. However, these techniques have only been demonstrated for estimating the skull and brain conductivities. Moreover, the method presented in [27] which uses only EEG data requires computational effort to converge, reported to be in the order of days by the authors. Using ROM-pEIT allows all compartments to be estimated simultaneously in a reasonable time frame.

The computational costs of ESI related methods become particularly prohibitive when performing sensitivity analyses, where effects of conductivity uncertainty in specific head tissues is explored. One way this problem has been circumvented is through the use of generalized Polynomial Chaos (gPC) expansions, where a result distribution is described by a linear combination of multivariate orthogonal polynomial basis functions and corresponding coefficients [8, 32]. Similarly to ROM, this method involves the calculation of the model output at multiple points on a sparse grid with specific parameters required to weight the coefficients. This technique was utilised by Schmidt et al. (2015) [32] for a sensitivity analysis in transcranial Direct Current Stimulation (tDCS) and by Vorwerk et al. (2019) [8] in EEG. Generalised PC has also been used for a conductivity uncertainty analysis in transcranial magnetic stimulation (TMS) and tDCS by Saturnino et al. (2019) [33]. Although resulting in an essential reduction in computational effort for these experiments, they still required the evaluations of the full FP at hundreds of points in parameter space for gPC convergence. The framework we present requires only a few dozen full order FP evaluations to reach a low RE in the FPs and IPs.

A closely related work by Maksymenko et al. (2020) also demonstrates a reduced order technique for fast solutions of the EEG FP [34]. Similarly, this framework used a set of full-order solutions at points in parameter space chosen via a greedy algorithm. This model could generate approximate lead field matrices for any conductivity set in parameter space very rapidly. There are, however, some notable differences between this framework and the one that we present in this work. Firstly, the implementation differs, where the former is applied to the EEG FP and solved using the Boundary Element Method with a small number of nodes in a model with 3 tissue compartments. Although it is suggested that it could equally be applied to FEM, this is not shown. Fundamentally, we present a rigorous *a posteriori* bound on the error in the reduced FP solution, and explicitly show this using a set of samples across the parameter space. Whereas, in the aforementioned publication [34], the error is not properly bounded.

Similarly, work by Codecasa et al. (2016) [35] has merged the techniques of ROM and gPC to perform an uncertainty analysis in TMS, where the model order reduction is used to guide the selection of the conductivity samples used for the polynomial chaos expansion. This work resulted in a significant speed up over gPC with regression, demonstrating the power of reduced order model techniques. There are a few differences in our work that make it distinguishable from this, such as a bound on the approximation error, application to pEIT, and the investigation of 3 additional tissues (scalp, compact skull and spongiform skull).

For studies involving gPC, where a model is trained using hundreds of support points, all were sensitivity analyses. Due to the nature of this work it is essential to have a highly trained model. However, for personalised conductivity field reconstruction, there is more interest in reducing the time from measurement to result. This is one of the strengths of ROM-pEIT. Shown in Figs. 5 and 6, only $10 - 30$ support points per injection pattern are required for accurate estimations in all tissues.

McCann et al. (2019) showed that spongiform bone varies between subjects and measurement techniques and that few attempts have been made to measure the conductivity of this tissue *in vivo*. Fernández-Corazza et al. (2017) [14] used pEIT but with a significant standard deviation and Aydin

et al. (2014) [30] used the pre-EEG calibration method. The latter found a spongiform conductivity of 84 mS/m [30] while the former found 173 ± 151 mS/m [14]. In the case of the former, a mixture of random error and numerical error (both present when using real data) may be responsible for the large standard deviation, however, the comparisons we draw above only consider numerical error. Clearly, *in vivo* measurements of spongiform bone have been challenging and the distribution of conductivity of this tissue among the population remains poorly understood as a result. The framework that we present is able to estimate spongiform bone to a high level of precision *in vivo* at the frequencies used for ESI, which as of writing has not been achieved by any other validated method in the literature. Furthermore, to the best of our knowledge, only two studies on non-invasive *in vivo* estimations of the CSF are present in the literature, with large errors in the estimations reported [36, 37].

A key feature of this work is the certified upper bound on the error in the FP. Although it guarantees a maximum error for each snapshot number, its usefulness as a stopping criteria is limited given the sharpness of the bound. A further challenge is that drawing a connection between the error in the FP and IP is not trivial. However, from Figs. 5 and 6 it is clear that optimal performance was achieved after 30 snapshots. Additionally, when the error between the full-order and the RB signal becomes much smaller than the noise, eq. (1) becomes approximately the norm of the noise over the electrodes. Relative to the measurements, that becomes approximately $4 - 5 \times 10^{-6}$ RE($\boldsymbol{\sigma}$) (for the noise we have used), which on Fig. 4 corresponds to about 30 snapshots, as observed in the IP. For our head model, this connects the observations in the FPs and IPs and therefore we suggest 30 snapshots as the optimal number and this can serve as a stopping criteria. However, this could change between participants, and more work is needed to confirm how variable this would be.

A time penalty incurred by ROM is the computational cost associated with training the stability factor interpolant during the offline phase, requiring multiple solutions to a generalised eigenvalue problem. This process takes approximately 15-30 minutes per problem (for an Intel Xeon CPU at 2.8 GHz for our model) and can be parallelised on a cluster. The interpolant generated is source vector independent, and therefore can be used for all electrode pairs. Although small in comparison to the training for ROM and the traditional method, this should still be considered as part of the offline training process. There exists some techniques that minimise the computational load of this stage such as greedy algorithms to reduce the number of interpolation points needed [38]. Exploring these optimisations of the framework will be work for the future. Further, we've found that interpolating between these points in a 6-dimensional space is a non-trivial task due to the complexity of the resulting manifold and the possible noise in the interpolation data. We found that the use of too many randomly selected interpolation points led to over-fitting and consequently a poor interpolation. The more conservative strategies suggested by Manzoni et al. (2015) [38] may help tackle this class of problem and this shall be explored in future work.

In this framework, we use the L2-norm in both the $\Delta_{RE}(\boldsymbol{\sigma})$ and the projection due to its ease of implementation. However, an equally valid $\Delta_{RE}(\boldsymbol{\sigma})$ can also be calculated using the norm of the space containing the solution [16]. The solution to the variational formulation of the problem can be found in an appropriate quotient Hilbert space, equipped with a norm that can be used for this task [17]. Modifying our framework to utilise this norm may improve the sharpness of the bound.

McCann et al. (2022) also investigated the effect of sutures on the EEG FP and IP and found that omission of the sutures from a head model led to significant source localisation errors [2]. It is unclear how the inclusion of sutures in a realistic head model may affect the training of the reduced order model, however this should be considered in future models. Moreover, with the possibility of estimating inner tissue compartments, the impact of including sutures on the estimation of the inner compartments could be assessed.

TDCS has been shown to produce a greater intensity and focality of the electric current at a point

of interest when highly accurate head models are considered [10] and optimal injection patterns are generated [39]. ROM could reduce the time constraints involved and in an online process estimate the conductivities and optimal injection patterns together almost instantly. Future work could involve producing a pipeline for TDCS such that the number of measurements taken from the patient are kept to a minimum.

One artefact of the training noticed was the loss of orthogonality in the transformation matrix after approximately 150 snapshots. This could be due to numerical errors introduced into the Gram-Schmidt orthonormalisation. We use the classical Gram-Schmidt process in this work, however, a well known and more numerically stable method called the modified Gram-Schmidt method could also be used [40]. Other numerically stable implementations of the Gram-Schmidt process have been developed and these may be explored in the future [41].

An additional substantial speed-up was achieved in the greedy algorithm by utilising the reduced model at each iteration to provide an initial guess for the PCG method when solving for a snapshot. As snapshots are added to the reduced model, the initial guess improves which leads to faster PCG solutions. Practically, this means that the time taken for one snapshot is halved after approximately 40 snapshots.

In conclusion, this new framework embodies a fresh approach to pEIT that will change its accessibility and reliability, recasting its role in the generation of personalised realistic head models used for ESI methods.

The software developed for this research can be found here: https://github.com/09nwalkerm/ROMpEIT.

References

[1] C. M. Michel and D. Brunet, "EEG Source Imaging: A Practical Review of the Analysis Steps," *Frontiers in Neurology*, vol. 10, p. 325, 2019.

[2] H. McCann and L. Beltrachini, "Impact of skull sutures, spongiform bone distribution, and aging skull conductivities on the EEG forward and inverse problems," *Journal of Neural Engineering*, vol. 19, p. 016014, 2022.

[3] F. Vatta et al., "Realistic and Spherical Head Modeling for EEG Forward Problem Solution: A Comparative Cortex-Based Analysis," *Computational Intelligence and Neuroscience*, vol. 2010, pp. 1–11, 2010.

[4] O. Puonti et al., "Accurate and robust whole-head segmentation from magnetic resonance images for individualized head modeling," *NeuroImage*, vol. 219, p. 117044, 2020.

[5] H. McCann, G. Pisano, and L. Beltrachini, "Variation in Reported Human Head Tissue Electrical Conductivity Values," *Brain Topography*, vol. 32, pp. 825–858, 2019.

[6] J. Haueisen et al., "The Influence of Brain Tissue Anisotropy on Human EEG and MEG," *NeuroImage*, vol. 15, pp. 159–166, 2002.

[7] R. Pohlmeier et al., "The influence of skull-conductivity misspecification on inverse source localization in realistically shaped finite element head models," *Brain Topography*, vol. 9, pp. 157–162, 1997.

[8] J. Vorwerk et al., "Influence of Head Tissue Conductivity Uncertainties on EEG Dipole Reconstruction," *Frontiers in Neuroscience*, vol. 13, p. 531, 2019.

[9] C. Wolters et al., "Influence of tissue conductivity anisotropy on EEG/MEG field and return current computation in a realistic head model: A simulation and visualization study using high-resolution finite element modeling," *NeuroImage*, vol. 30, pp. 813–826, 2006.

[10] S. Wagner et al., "Investigation of tDCS volume conduction effects in a highly realistic head model," *Journal of Neural Engineering*, vol. 11, p. 016002, 2014.

[11] H. McCann and L. Beltrachini, "Does participant's age impact on tDCS induced fields? Insights from computational simulations," *Biomedical Physics & Engineering Express*, vol. 7, p. 045018, 2021.

[12] D. Holder, ed., *Electrical Impedance Tomography*. CRC Press, 0 ed., 2004.

[13] M. Fernández-Corazza et al., "Effects of Head Model Inaccuracies on Regional Scalp and Skull Conductivity Estimation Using Real EIT Measurements," in *II Latin American Conference on Bioimpedance* (F. Simini and P. Bertemes-Filho, eds.), vol. 54, pp. 5–8, 2016. Series Title: IFMBE Proceedings.

[14] M. Fernández-Corazza et al. "Skull Modeling Effects in Conductivity Estimates Using Parametric Electrical Impedance Tomography," *IEEE Transactions on Biomedical Engineering*, vol. 65, pp. 1785–1797, 2018.

[15] M. Fernández-Corazza et al., "Analysis of parametric estimation of head tissue conductivities using Electrical Impedance Tomography," *Biomedical Signal Processing and Control*, vol. 8, pp. 830–837, 2013.

[16] A. Quarteroni, A. Manzoni, and F. Negri, *Reduced Basis Methods for Partial Differential Equations*, vol. 92 of *UNITEXT*. Cham: Springer International Publishing, 2016.

[17] E. Somersalo, M. Cheney, and D. Isaacson, "Existence and Uniqueness for Electrode Models for Electric Current Computed Tomography," *SIAM Journal on Applied Mathematics*, vol. 52, no. 4, pp. 1023–1040, 1992.

[18] M. Fernández-Corazza, N. von Ellenrieder, and C. H. Muravchik, "Estimation of electrical conductivity of a layered spherical head model using electrical impedance tomography," *Journal of Physics: Conference Series*, vol. 332, p. 012022, 2011.

[19] P. Vauhkonen et al., "Three-dimensional electrical impedance tomography based on the complete electrode model," *IEEE Transactions on Biomedical Engineering*, vol. 46, pp. 1150–1160, 1999.

[20] Kuo-Sheng Cheng et al., "Electrode models for electric current computed tomography," *IEEE Transactions on Biomedical Engineering*, vol. 36, pp. 918–924, 1989.

[21] P. J. Vauhkonen, M. Vauhkonen, and J. P. Kaipio, "Fixed-lag smoothing and state estimation in dynamic electrical impedance tomography," *International Journal for Numerical Methods in Engineering*, vol. 50, pp. 2195–2209, 2001.

[22] B. Aubert-Broche, A. C. Evans, and L. Collins, "A new improved version of the realistic digital brain phantom," *NeuroImage*, vol. 32, pp. 138–145, 2006.

[23] H. Elman, D. Silvester, and A. Wathen, *Finite Elements and Fast Iterative Solvers: with Applications in Incompressible Fluid Dynamics*. Oxford University PressOxford, 2 ed., 2014.

[24] L. Beltrachini, "The analytical subtraction approach for solving the forward problem in EEG," *Journal of Neural Engineering*, vol. 16, p. 056029, 2019.

[25] J. E. Dennis and R. B. Schnabel, *Numerical Methods for Unconstrained Optimization and Nonlinear Equations*. Society for Industrial and Applied Mathematics, 1996.

[26] M. Dannhauer et al., "Modeling of the human skull in EEG source analysis," *Human Brain Mapping*, vol. 32, pp. 1383–1399, 2011.

[27] Z. Akalin Acar, C. E. Acar, and S. Makeig, "Simultaneous head tissue conductivity and EEG source location estimation," *NeuroImage*, vol. 124, pp. 168–180, 2016.

[28] F. Costa et al., "Skull Conductivity Estimation for EEG Source Localization," *IEEE Signal Processing Letters*, vol. 24, pp. 422–426, 2017.

[29] C. H. Wolters et al., "Combined EEG/MEG source analysis using calibrated finite element head models," *Biomedizinische Technik/Biomedical Engineering. Rostock, Germany: Walter de Gruyter*, vol. 55, no. Suppl 1, pp. 64–68, 2010. Publisher: Citeseer.

[30] Ü. Aydin et al., "Combining EEG and MEG for the Reconstruction of Epileptic Activity Using a Calibrated Realistic Volume Conductor Model," *PLoS ONE*, vol. 9, p. e93154, 2014.

[31] M. Antonakakis et al., "Inter-Subject Variability of Skull Conductivity and Thickness in Calibrated Realistic Head Models," *NeuroImage*, vol. 223, p. 117353, 2020.

[32] C. Schmidt et al., "Impact of uncertain head tissue conductivity in the optimization of transcranial direct current stimulation for an auditory target," *Journal of Neural Engineering*, vol. 12, p. 046028, 2015.

[33] G. B. Saturnino et al., "A principled approach to conductivity uncertainty analysis in electric field calculations," *NeuroImage*, vol. 188, pp. 821–834, 2019.

[34] K. Maksymenko, M. Clerc, and T. Papadopoulo, "Fast Approximation of EEG Forward Problem and Application to Tissue Conductivity Estimation," *IEEE Transactions on Medical Imaging*, vol. 39, pp. 888–897, 2020.

[35] L. Codecasa et al., "Fast MOR-Based Approach to Uncertainty Quantification in Transcranial Magnetic Stimulation," *IEEE Transactions on Magnetics*, vol. 52, pp. 1–4, 2016.

[36] T. Ouypornkochagorn and S. Ouypornkochagorn, "In Vivo Estimation of Head Tissue Conductivities Using Bound Constrained Optimization," *Annals of Biomedical Engineering*, vol. 47, pp. 1575–1583, 2019.

[37] T. Ferree, K. Eriksen, and D. Tucker, "Regional head tissue conductivity estimation for improved EEG analysis," *IEEE Transactions on Biomedical Engineering*, vol. 47, pp. 1584–1592, 2000.

[38] A. Manzoni and F. Negri, "Heuristic strategies for the approximation of stability factors in quadratically nonlinear parametrized PDEs," *Advances in Computational Mathematics*, vol. 41, pp. 1255–1288, 2015.

[39] R. J. Sadleir et al., "Target Optimization in Transcranial Direct Current Stimulation," *Frontiers in Psychiatry*, vol. 3, 2012.

[40] Å. Björck, "Numerics of Gram-Schmidt orthogonalization," *Linear Algebra and its Applications*, vol. 197-198, pp. 297–316, 1994.

[41] E. Carson et al., "Block Gram-Schmidt algorithms and their stability properties," *Linear Algebra and its Applications*, vol. 638, pp. 150–195, 2022.